Title

Pervasive cortical and white matter anomalies in a mouse model for CHARGE syndrome

Journal

Journal of Anatomy, 243(1)

ISSN

0021-8782

Authors

Donovan, Alex PA
Rosko, Lauren
Ellegood, Jacob
et al.

Publication Date

2023-07-01

DOI

10.1111/joa.13856

Received: 30 August 2022 | Revised: 31 January 2023 | Accepted: 17 February 2023

DOI: 10.1111/joa.13856

Journal of Anatomy ANATOMICAL SOCIETY WILEY

ORIGINAL ARTICLE

Pervasive cortical and white matter anomalies in a mouse model for CHARGE syndrome

Alex P. A. Donovan[1] | Lauren Rosko[2,3] | Jacob Ellegood[4] | Yushi Redhead[1] | Jeremy B. A. Green[1] | Jason P. Lerch[4,5,6,7] | Jeffrey K. Huang[2,3,8] | M. Albert Basson[1,9]

[1]Centre for Craniofacial and Regenerative Biology, King's College London, London, UK

[2]Department of Biology, Georgetown University, Washington, DC, USA

[3]Interdisciplinary Program in Neuroscience, Georgetown University, Washington, DC, USA

[4]Mouse Imaging Centre, The Hospital for Sick Children, Toronto, Ontario, Canada

[5]Department of Medical Biophysics, The University of Toronto, Toronto, Ontario, Canada

[6]Department of Neurosciences and Mental Health, The Hospital for Sick Children, Toronto, Ontario, Canada

[7]Department of Preclinical Imaging, Wellcome Centre for Integrative Neuroimaging, University of Oxford, Oxford, UK

[8]Centre for Cell Reprogramming, Georgetown University, Washington, DC, USA

[9]MRC Centre for Neurodevelopmental Disorders, King's College London, London, UK

Correspondence
M. Albert Basson, Centre for Craniofacial and Regenerative Biology, King's College London, Floor 27, Guy's Hospital Tower Wing, London SE1 9RT, UK.
Email: albert.basson@kcl.ac.uk

Funding information
Anatomical Society; CHARGE syndrome Foundation

Abstract

CHARGE (Coloboma of the eye, Heart defects, Atresia of the choanae, Retardation of growth, Genital anomalies and Ear abnormalities) syndrome is a disorder caused by mutations in the gene encoding CHD7, an ATP dependent chromatin remodelling factor, and is characterised by a diverse array of congenital anomalies. These include a range of neuroanatomical comorbidities which likely underlie the varied neurodevelopmental disorders associated with CHARGE syndrome, which include intellectual disability, motor coordination deficits, executive dysfunction, and autism spectrum disorder. Cranial imaging studies are challenging in CHARGE syndrome patients, but high-throughput magnetic resonance imaging (MRI) techniques in mouse models allow for the unbiased identification of neuroanatomical defects. Here, we present a comprehensive neuroanatomical survey of a *Chd7* haploinsufficient mouse model of CHARGE syndrome. Our study uncovered widespread brain hypoplasia and reductions in white matter volume across the brain. The severity of hypoplasia appeared more pronounced in posterior areas of the neocortex compared to anterior regions. We also perform the first assessment of white matter tract integrity in this model through diffusion tensor imaging (DTI) to assess the potential functional consequences of widespread reductions in myelin, which suggested the presence of white matter integrity defects. To determine if white matter alterations correspond to cellular changes, we quantified oligodendrocyte lineage cells in the postnatal corpus callosum, uncovering reduced numbers of mature oligodendrocytes. Together, these results present a range of promising avenues of focus for future cranial imaging studies in CHARGE syndrome patients.

1 | INTRODUCTION

Haploinsufficiency of the gene *CHD7*, encoding an ATP-dependent chromatin remodelling factor, is the cause of approximately 90% of CHARGE syndrome cases (Janssen et al., 2012; Vissers et al., 2004). CHARGE syndrome is a congenital condition with an estimated prevalence of between 0.1–1.2 in every 10,000 live births (Blake & Prasad, 2006). Although particularly phenotypically heterogeneous, CHARGE syndrome is characterized by variable combinations of a core constellation of phenotypes, which include: Coloboma of the eye, Heart defects, Atresia of the choanae, Retardation of growth, Genital anomalies and Ear abnormalities. Although clinically defined according to these phenotypes as major diagnostic criteria, a number of minor associated phenotypes are also frequently noted (Blake et al., 1998; Verloes, 2005). Amongst these are a wide array of neuropsychiatric conditions, including intellectual disability (Blake & Prasad, 2006), executive dysfunction (Hartshorne et al., 2007; Nicholas, 2005) and autism spectrum disorders (Bernstein & Denno, 2005; Hartshorne et al., 2005; Johansson et al., 2005; Smith et al., 2005; Wachtel et al., 2007).

Although these neuropsychiatric disorders have been associated with CHARGE syndrome, it has been difficult to identify specific structural brain phenotypes that may underlie these conditions. This is widely due to the lack of large scale MRI studies describing differences in structure between the brains of people with CHARGE and neurotypical individuals (de Geus et al., 2017). However, phenotypes in the central nervous systems of individuals with CHARGE syndrome have been noted. These include: Cranial nerve hypoplasia (Hoch et al., 2017; Lin et al., 1990; Shiohama et al., 2019), cerebellar hypoplasia (Hoch et al., 2017; Shiohama et al., 2019; Sohn et al., 2016; Yu et al., 2013), ventriculomegaly (Hoch et al., 2017), arhinencephaly/holoprosencephaly (Lin et al., 1990), white matter and corpus callosum deficits (Chen et al., 2019; Gregory et al., 2013; Shiohama et al., 2019), decreased basal ganglia volume (Shiohama et al., 2019) and frontal lobe hypoplasia (Gregory et al., 2013). For all the diversity of neuroanatomical phenotypes described, studies are continually emerging noting new observations in the central nervous system of individuals with CHARGE syndrome. The sporadic nature of cranial imaging studies and low numbers of patient participants highlights the need to study animal models of the disorder. This is exemplified by the fact that even in the case of cerebellar hypoplasia, which is now one of the most common observations in the brains of CHARGE syndrome patients, few cases were noted until a role for *CHD7* in the development of the murine hindbrain was uncovered (Yu et al., 2013), which subsequently stimulated focused cranial imaging studies into cerebellar defects in CHARGE patients.

Despite this valuable role for mouse models in identifying neuroanatomical defects, analysis of brain structure and volume in mice has in the past been slow due to the laborious nature of brain collection, sectioning, imaging and quantification. However, more recently the use of ex-vivo magnetic resonance and diffusion tensor imaging (MRI/DTI) has proven to be an effective high throughput method for neuroanatomical phenotyping of mouse models (Ellegood et al., 2018; Lerch et al., 2017). Indeed, these methods have already proven fruitful in the identification of neuroanatomical defects arising from loss of CHD7 function (Donovan et al., 2017; Whittaker, Kasah, et al., 2017). Studies in models of CHARGE syndrome have unveiled diverse disruptions in brain volume, including extensive cerebellar hypoplasia (Donovan et al., 2017; Feng et al., 2017; Whittaker, Kasah, et al., 2017; Whittaker, Riegman, et al., 2017; Yu et al., 2013) resultant of *Chd7* knockout in the cerebellar anlage and substantial midbrain hypolasia (Donovan et al., 2017) when *Chd7* was deleted from the embryonic mid-hindbrain region. These models are particularly valuable when studying phenotypically variable disorders such as CHARGE syndrome, as inbred lines provide a homogeneity to the genetic background. These tools together provide a powerful and unbiased method for the identification of novel neuroanatomical correlates, which can subsequently be explored in patients through focused high-power cranial imaging studies.

Here, we use high-resolution 7 T structural MRI and DTI to comprehensively map neuroanatomical defects present in $Chd7^{Gt/+}$ mice, a haploinsufficient model proven to reflect many phenotypes present in CHARGE syndrome. We find widespread defects in brain volume including a substantial loss of white matter across numerous brain regions. DTI and immunostaining of oligodendrocyte lineage cells indicated functional white matter abnormalities and reduced numbers of oligodendrocyte lineage cells in these mice.

2 | MATERIALS AND METHODS

2.1 | Mice

Mice were bred and maintained according to official Home Office regulations in the New Hunt's House Biological Services Unit, King's College London. The day of birth was considered postnatal day 0 (P0). B6D2F1 mice were generated by crossing male DBA/2 J with female C57BL/6J mice. $Chd7^{xk403/+}$ ($Chd7^{Gt/+}$) (Randall et al., 2009) heterozygous mice were maintained on a B6D2F1 (C57BL/6J × DBA/2 J F1) background. Ear punch DNA preparations were genotyped by PCR using primers outlined in the original publications. All procedures were performed in accordance with the UK Home Office Animals Scientific Procedures Act 1986.

2.2 | Tissue preparation for magnetic resonance imaging

Mice were terminally anaesthetised with 150 mg/kg pentobarbital sodium via intra-peritoneal (IP) injection. They were then fixed to a perfusion board and the chest cavity was opened. A needle was inserted into the left ventricle of the heart and an incision made in

the right atrium. A trans-cardiac perfusion flush using 30 mL of room temperature 1xPBS with 1 μL/mL heparin and 2 mM ProHance contrast reagent (Bracco, 0270-1111-04) was carried out, at a flow rate of 1 mL/min using a motorised peristaltic pump. Subsequently, mice were perfused with 30 mL of room temperature 4% PFA with 2 mM ProHance, at the same flow rate of 1 mL/min. After perfusion fixation, the head, skin and eyes were removed, the zygomatic bone was cut, and the lower jaw was dissected out. Immediately after dissection, the prepared skull/brain was placed in 10 mL of 4% PFA with 2 mM ProHance and left rocking overnight at 4°C. The following day the skull/brain was washed out of PFA into 1XPBS with 2 mM ProHance and 0.02% sodium azide and stored at 4°C for at least 1 month before MRI scanning.

2.3 | Magnetic resonance imaging (MRI)

MRI scanning of adult (P60) *Chd7*$^{Gt/+}$ mice (n = 11) and wildtype controls (n = 12) was performed on a multi-channel 7 T MRI scanner (Agilent), which imaged fixed brains in skulls. Brains were imaged in parallel using 16 custom-built solenoid coils (Lerch et al., 2011). Parameters used for the anatomical MRI scanning are detailed in Donovan et al. (2017) and Whittaker, Kasah, et al. (2017). For Diffusion Tensor Imaging (DTI) imaging a 3D diffusion weighted fast spin echo sequence (FSE), with an echo train length of 6 was used. Parameters for the DTI sequence were: TR = 270 ms, first TE = 32 ms, and a TE of 10 ms for the remaining 5 echoes, 1 average. Field-of-view (FOV) of 14 × 14 × 25 mm^3 and a matrix size of 180 × 180 × 324 yielding an image with 78 μm isotropic voxels. Five b = 0 s/mm^2 images and 30 high b-value (b = 2147 s/mm^2) in 30 different directions were acquired using the Jones30 scheme (Jones et al., Magnetic Resonance in Medicine, 1999). Total imaging time was ~12 h. After acquisition the images were analyzed using the FSL software package (FMRIB, Oxford UK), with was used to create fractional anisotropy (FA), mean diffusivity (MD), axial diffusivity (AD), and radial diffusivity (RD) maps for each of the brains used in this study.

To visualize anatomical differences the anatomical images collected (or b = 0 s/mm^2 images for DTI) were linearly and non-linearly registered together then aligned to each other to create a population atlas of the average anatomy of the entire study group. The anatomy of each mouse brain was then individually registered to the population atlas to automatically calculate regional and voxel-wise volumetric differences in an unbiased fashion. Note the 40 μm anatomical images and the b = 0 s/mm^2 DTI images are registered separately.

These analyses were performed using a combination of MRI autoreg tools and advanced normalization tools (Described in Ellegood et al., 2018). For the volume measurements, the deformations needed to take each individual mouse's anatomy into this final atlas space were measured. The goal being to model how the deformation fields relate to genotype (Lerch et al., 2008; Nieman et al., 2006). The jacobian determinants of the deformation fields are then calculated as measures of volume at each voxel. For the diffusion measurements, the registration allows for the analysis of the intensity differences of all measures (FA, MD, AD, and RD) between genotypes.

Significant volume changes and intensity differences can then be calculated by warping a pre-existing classified MRI atlas onto the population atlas, which allows for the volume or mean diffusion measure (FA, MD, AD, and RD) (Lerch et al., 2008). This atlas is comprised of three atlases and results in a map of 159 independent structures, allowing for the labelling of structures and allocation of voxel-wise volumetric changes across the brain (Dorr et al., 2008; Ellegood et al., 2018; Lerch et al., 2000; Steadman et al., 2014; Ullmann et al., 2013). Absolute and relative volumetric changes were calculated, and false discovery rate (FDR) calculations were performed to assess for statistical significance whilst accounting for multiple comparisons.

2.4 | Skull morphometric analysis

Mouse crania were prepared for MRI by the methods outlined, then scanned in a Scanco 197 μCT50 (Scanco medical). Samples were scanned at 90 kV, 88 μA, with a 198 0.5-mm aluminium filter, 303 ms integration time, no averaging, and images captured every 199 0.36° though 180° rotation. Specific parameters were calculated from whole -skull scans at a 200 voxel resolution of 10 μm. Reconstructions and analyses were performed using Scanco 201 software. Skull morphometric analysis was performed as outlined in Toussaint et al. (2021). 202 Briefly, the locations of 68 anatomical landmarks were placed onto the three -dimensional 203 reconstructions of mouse skulls derived from μCT scanning. Mandible landmarks were not 204 placed, as these structures were removed by dissection in preparation for MRI/DTI scanning. 205 To calculate skull sizes the distances of these anatomical landmark points from a defined 206 centroid were measured.

2.5 | Immunohistochemistry

Brains were cryoprotected in 30% sucrose before freezing in optimal cutting temperature medium (Sakura) on dry ice, then stored at −80°C. 12 μm sections of brain were sectioned on a cryostat and mounted on SuperFrostPlus slides. After drying slides for 1 h at room temperature (RT), slides were incubated in antigen unmasking solution for 30 min at 95°C (Vector laboratories). Slides were incubated in blocking solution (10% goat serum, 1% donkey serum, 0.25% triton in TBS) for 1 h at RT. For mouse antibodies, an extra 1 hr of mouse-on-mouse blocking reagent (Vector laboratories) was used. Primary and secondary antibodies were diluted in blocking solutions. Primary antibodies for IHC were as follows: rabbit Olig2 (1:300, Millipore Cat# MABN50, RRID: AB_10807410), mouse CC1 (1:200; Milipore Cat# OP80, RRID: AB_2057371), mouse NKX2.2 (1:100, DSHB Cat# 74.5A5, RRID: AB_531794), rat MBP (1:300; Biorad Cat# aa82-87; RRID: AB_325004), chicken GFAP (1:500; Aves GFAP;

RRID: AB_23547), rabbit Sox9 (1:500; Millipore cat# AB5535; RRID: AB_2239761). Images were collected on a Zeiss LSM 800 confocal microscope. Quantification of immunostaining was done by 1 blinded investigator using the ImageJ cell counter manually. For corpus callosum imaging, one medial and two lateral images of corpus callosum and cingulum were taken from 3 sections per slide ($n = 4$). Density per square millimeter was calculated in Microsoft Excel as previously described in Chamberlain et al., 2017. All statistics were performed using Prism. Data are expressed as mean ± SEM. Comparisons were analyzed by two-tailed t-tests. Statistical significance is reported as $^{*}p \leq 0.05$, $^{**}p \leq 0.01$, $^{***}p \leq 0.001$.

3 | RESULTS

3.1 | Extensive hypoplasia across the brains of adult *Chd7*$^{Gt/+}$ mice

We previously reported specifically on reduced volumes in the neocortex and cerebellum of adult (P60) *Chd7*$^{Gt/+}$ mice by high-resolution 7 T structural MRI (Whittaker, Kasah, et al., 2017). We extended the analysis of this data to encompass a total of 168 regions of the brain, the maximum defined within the most comprehensive reference atlas available (Figure 1). Strikingly, all regions

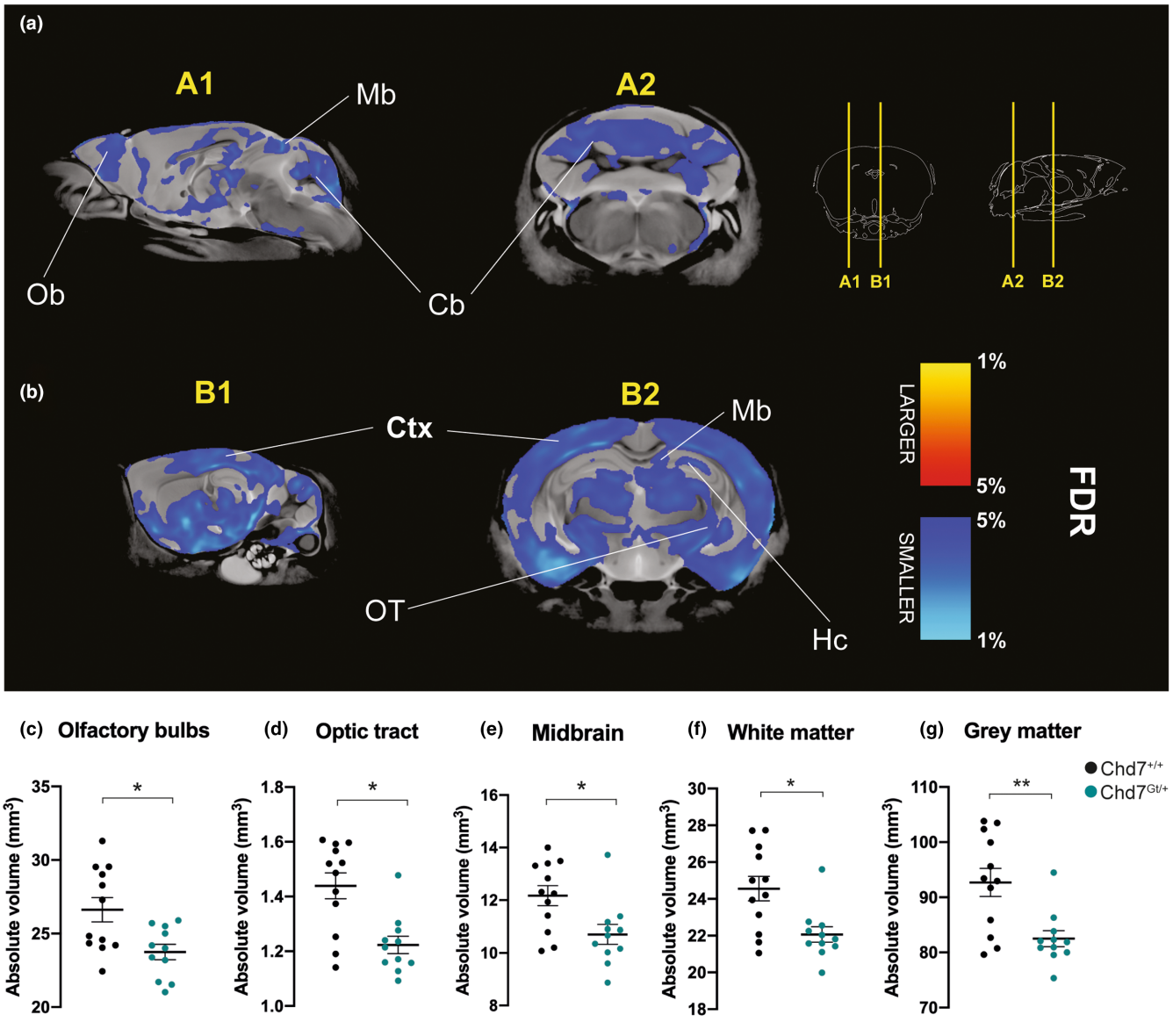

FIGURE 1 Widespread hypoplasia in the brains of adult *Chd7*$^{Gt/+}$ mice. (a) Sagittal (A1/B1) and coronal (A2/B2) slice images from high-resolution 7 T structural MRI of adult (P60) *Chd7*$^{+/+}$ ($n = 12$) and *Chd7*$^{Gt/+}$ ($n = 11$) mice, slices shown are lateral (A1), medial (B1), posterior (A2) and central (B2). Absolute volumetric differences relative to *Chd7*$^{+/+}$ are coloured according to the false discovery rate (FDR) scale from 1% to 5% FDR. (c–g) Absolute volumetric differences (mm^3) between *Chd7*$^{+/+}$ (black) and *Chd7*$^{Gt/+}$ (teal) mice for the Olfactory bulbs (c), Optic tract (d), Midbrain (e), total white matter (f) and total grey matter (g), between *Chd7*$^{+/+}$ (black) and *Chd7*$^{Gt/+}$ (teal) mice. Regions of interest in (a) are labelled as follows, Cb, cerebellum; Ctx, cortex; Hc, hippocampus; Mb, midbrain; Ob, olfactory bulb; OT, optic tract. All graphs are represented as mean ± SEM. Each point represents a biological replicate. *FDR <5%, **FDR <1%.

measured displayed some degree of volume reduction, with 128 being statistically significant ($p < 0.05$, FDR < 5%) and no regions exhibiting increases in absolute volume (Table S1). In addition to our previous findings in specific cerebellar lobules, this included several hypoplastic regions consistent with previous studies in other mouse models of *Chd7* deficiency: we saw reduced olfactory bulbs (Bergman et al. 2010; Layman et al. 2009) (−10.72%, Figure 1c), optic tract (Gage et al., 2015) (−15.00%, Figure 1d) and midbrain (Donovan et al., 2017) (−12.04%, Figure 1e) (Table 1). There was also a significant loss of both total white matter (−10.15%, Figure 1f) and grey matter (−10.98%, Figure 1g) volumes.

3.2 | Adult *Chd7*$^{Gt/+}$ mice have normal skull sizes

The development and growth of the brain and skull are coordinated, and reductions in cranial volume can underlie secondary defects in the growth of the brain (Richtsmeier and Flaherty, 2013). Thus, we asked if the size of the skull is altered in these mice. We scanned the skulls of the adult *Chd7*$^{Gt/+}$ mice that were prepared for MRI by micro-computed tomography (μCT) (Figure 2a). Intracranial volume was determined using a landmark-free morphometrics approach (Toussaint et al., 2021). Intracranial volumes were generated by measuring the mean distance of a point mesh of the internal surface of the cranium from their centroid. This analysis showed that adult *Chd7*$^{Gt/+}$ mice have normal skull sizes (Figure 2b), ruling out the possibility that the reduced brain volume in adult *Chd7*$^{Gt/+}$ mice is directly linked to reduced adult intracranial volume.

3.3 | Body weight abnormalities during early postnatal life in *Chd7*$^{Gt/+}$ mice

General growth defects during early life can have an immediate impact on the growth and maturation of the brain. To define whether defects in growth postnatally could contribute to the widespread brain hypoplasia we observed in adult *Chd7*$^{Gt/+}$ mice, we carried out a time course analysis of body weights from birth until adulthood (Figure 2c). A subset of mice sent for MRI scanning were weighed beforehand at postnatal day 60 (P60) and several cohorts of *Chd7*$^{Gt/+}$ and control mice were weighed at P0, P8, P14 and P21. No difference in body weight was present in *Chd7*$^{Gt/+}$ mice at P21 or P60, however at each of the earlier stages *Chd7*$^{Gt/+}$ mice had significantly reduced body weights (Figure 2c). This raises the possibility that brain volume abnormalities in these mice could at least in part be impacted by a retardation in body growth during the early postnatal period.

3.4 | *Chd7*$^{Gt/+}$ mice have a pronounced loss of volume in the cerebral cortex

Cranial imaging studies in CHARGE syndrome patients have previously revealed distinct but often subtle alterations in the volume of areas of the cerebral cortex (Gregory et al., 2013; Lin et al. 1990; Shiohama et al., 2019). Intriguingly, adult *Chd7*$^{Gt/+}$ mice had substantial hypoplasia across the cerebral cortex, including the prefrontal (−7.81%, Figure S1a), primary motor (−8.74%, Figure S1c), primary somatosensory (−6.88%, Figure S1d), primary auditory (−14.02%, Figure S1e) and primary visual (−15.78%, Figure S1f) cortices. This appeared to follow a trend by which the more posteriorly and medially situated cortical

TABLE 1 Volumetric abnormalities identified in this study that recapitulate previously identified phenotypes in mouse models of CHARGE syndrome and human patients with CHARGE syndrome.

Region	% difference in adult *Chd7*$^{Gt/+}$ mice	Phenotype previously identified	Identified in	References
Cerebellar	−14.49%	Cerebellar hypoplasia	Human and mouse	(Donovan et al., 2017; Feng et al., 2017; M. J. Hoch et al., 2017; Shiohama et al., 2019; Sohn et al., 2016; Whittaker, Riegman, et al., 2017; Yu et al., 2013)
Brainstem	−8.19%	Brainstem hypoplasia	Human	(M. J. Hoch et al., 2017)
Corpus callosum	−9.16%	Corpus callosum hypoplasia/agenesis	Human	(Chen et al., 2019; Gregory et al., 2013; Shiohama et al., 2019)
White matter	−10.15%	White matter loss	Human and mouse	(Chen et al., 2019; Gregory et al., 2013; He et al., 2016; Shiohama et al., 2019)
Optic tract	−15.00%	Optic tract hypoplasia	Human	(Johansson et al., 2005; Russell-Eggitt et al., 1990)
Basal ganglia	−11.43% to −17.22%	Decreased basal ganglia volume	Human and mouse	(Donovan et al., 2017; Shiohama et al., 2019)
Midbrain	−12.04%	Midbrain hypoplasia	Mouse	(Donovan et al., 2017)
Olfactory bulbs	−10.72%	Olfactory bulb hypoplasia/ isolated arhinencephaly	Human and mouse	(Layman et al., 2009; Sanlaville et al., 2006)
Frontal cortex	−6.26% to −15.78%	Frontal lobe hypoplasia	Human	(Gregory et al., 2013)

areas, such as the primary somatosensory, auditory and visual cortices, were more severely affected than those areas found more anteriorly such as the primary motor and frontal cortices (Figure 3a). To further address the heterogeneous nature of cortical hypoplasia in these mice and to establish the differences in the proportion of the cortex taken up by different cortical areas, we calculated the volume of each area of the cortex relative to the total cortical volume for each replicate (Figure 3b; Table S1). This analysis further confirmed the observation of progressively greater loss of volume as one moves from anterior to posterior (Figure 3b). When considered relative to the total volume of the cortex, some more anterior areas such as the frontal and primary somatosensory cortices in fact represented a larger proportion of the cortex in *Chd7*$^{Gt/+}$ mice compared to wild-type controls (Figure 3b). Conversely, areas at the posterior of the cortex, such as secondary auditory and primary visual cortices were diminished in the proportion of total cortical volume that they occupied (Figure 3b).

3.5 | Diminishment of white matter volume in *Chd7*$^{Gt/+}$ mice

Abnormalities in white matter development and maintenance have been identified in several mouse models with homozygous conditional deletion of *Chd7* from the oligodendrocyte lineage (He et al., 2016; Marie et al., 2018). These studies did not determine if *Chd7* haploinsufficiency, as found in CHARGE syndrome, can lead to white matter anomalies. Here, our analysis of *Chd7*$^{Gt/+}$ mice identified reduced volume of white matter structures throughout the brain, with a reduction in total white matter volume of 10.15% (Figure 1f). Hypoplasia was present in several of the major white matter tracts including the optic tract (−15.00%, Figure 4a), corpus callosum (−9.16%, Figure 4b) and habenular commissure (−12.76%, Figure 4c). The volume of the internal capsule, a tract which contains many of the long-range projections to and from the cerebral cortex, was also markedly reduced in volume by 13.97% (Figure 4d). *Chd7*$^{Gt/+}$ mice presented with a pronounced reduction in white matter volume across many subdivisions of the cerebellum (Figure 4e). This included loss of white matter in lobules I/II (−13.25%), III (−16.53%), IV/V (−13.41%), VI/VII (−13.03%), VIII (−14.88%) and IX (−12.24%), as well as Crus I (−17.83%) and II (−11.32%) (Figure 5e). This finding suggests that white matter defects could substantially contribute to previously described incidences of cerebellar hypoplasia, both in patients (Hoch et al., 2017; Shiohama et al., 2019; Sohn et al., 2016; Yu et al., 2013) and mouse models (Donovan et al., 2017; Feng et al., 2017; Whittaker, Kasah, et al., 2017; Whittaker, Riegman, et al., 2017; Yu et al., 2013).

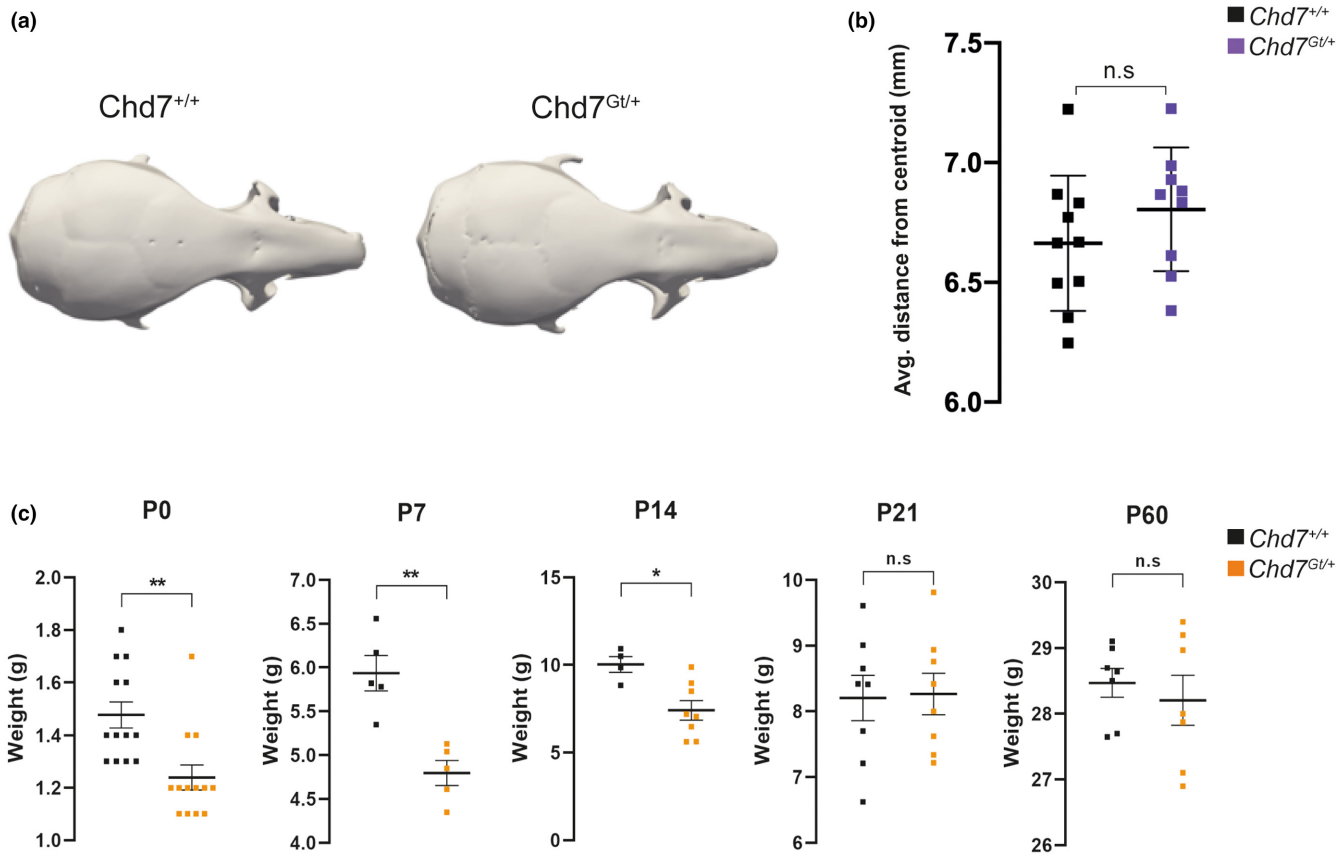

FIGURE 2 The effect of *Chd7* haploinsufficiency on skull size and body weight. (a) 3D reconstructions of μCT images from adult *Chd7*$^{+/+}$ and *Chd7*$^{Gt/+}$ mice, representative images for each genotype are shown. (b) Average distance from centroid in millimetres for *Chd7*$^{+/+}$ (black) and *Chd7*$^{Gt/+}$ (purple) mice. (c) Measurements of body weight in grams of *Chd7*$^{+/+}$ (black) and *Chd7*$^{Gt/+}$ (orange) mice. All graphs are represented as mean ± SEM. Each point represents a biological replicate. $^{*}p < 0.05$, $^{**}p < 0.01$.

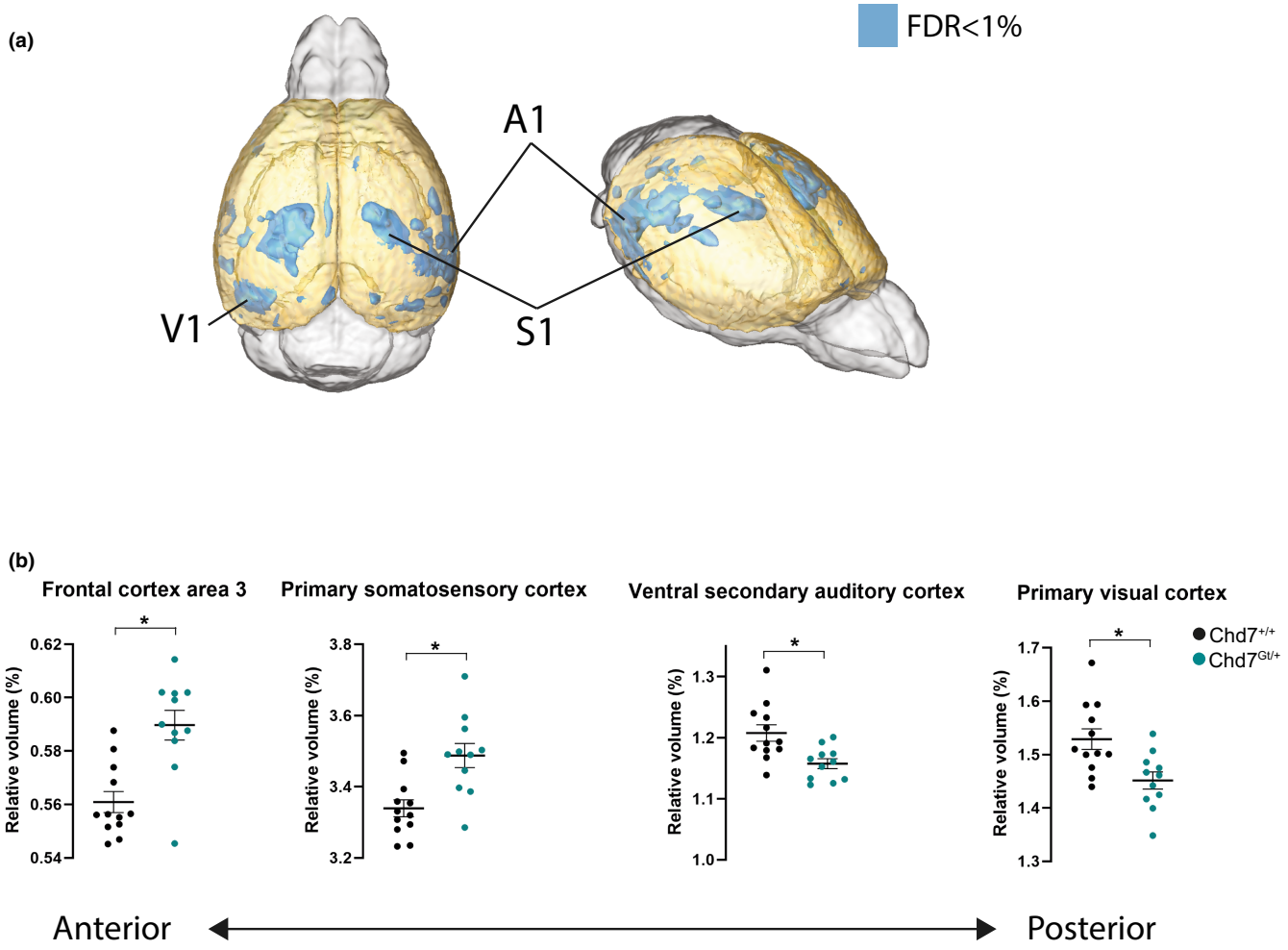

FIGURE 3 Cerebral cortical volume is altered in a region-specific manner in the brains of adult *Chd7*$^{Gt/+}$ mice. (a) 3D representation of cerebral cortical regions reduced in volume with an FDR of less than 1%, shown in blue. (b) Volumes relative to total cortical size (%) between *Chd7*$^{+/+}$ (black) and *Chd7*$^{Gt/+}$ (teal) mice for frontal cortex area 3, primary somatosensory cortex, ventral secondary auditory cortex and primary visual cortex, shown from anterior (left) to posterior (right). Regions of interest in (a) are labelled as follows, S1: primary somatosensory cortex, V1: primary visual cortex, A1: primary auditory cortex. All graphs are represented as mean ± SEM. Each point represents a biological replicate. *FDR < 5%, **FDR < 1%.

3.6 | Assessment of fiber tract microstructure using diffusion tensor imaging (DTI)

To determine whether the myelinated structures of the brain displayed indicators of microstructural anomalies, we used diffusion tensor imaging (DTI). DTI was performed on the same cohort of adult *Chd7*$^{Gt/+}$ and control mice as the MRI study. Of the 159 regions examined, no significant differences were found in fractional anisotropy, mean diffusivity or radial diffusivity in *Chd7*$^{Gt/+}$ mice when compared to controls (Figure 5). However, there were some regions within the hippocampal formation, optic tract, commissural tracts and cerebellum that trended ($p < 0.05$; FDR < 0.8) towards a decrease in fractional anisotropy, which denotes loss of water diffusion directionality indicative of white matter microstructural abnormalities due to disorganization of the white matter tract, axonal size, axonal number and/or a change in myelination. This analysis also identified increases in mean and radial diffusivity, measures of water diffusion indicating higher diffusion and hence loss of white matter organisation and integrity (Figure 5d–f). Within the hippocampal formation, the hippocampus and fimbria had decreases in fractional anisotropy and increases in radial diffusivity (Figure 5d–f), and the temporal association area had a decrease in fractional anisotropy (Figure 5d). The optic tract had both a decrease in fractional anisotropy and increases in both mean and radial diffusivity (Figure 5d–f). Within the cerebellum, the white matter of lobule X and the superior cerebellar peduncle displayed reductions in fractional anisotropy (Figure 5d), whilst the white matter of lobule VIII presented with increases in both mean and radial diffusivity (Figure 5e,f). The white matter of cerebellar lobules IX and X had increases in radial (Figure 5f) and mean (Figure 5e), respectively. Within the major commissural tracts, the corpus callosum exhibited both a decrease in fractional anisotropy (Figure 5d) and increases in mean and radial diffusivity (Figure 5e,f), whilst the posterior commissure displayed only increases in mean and radial diffusivity (Figure 5e,f). These

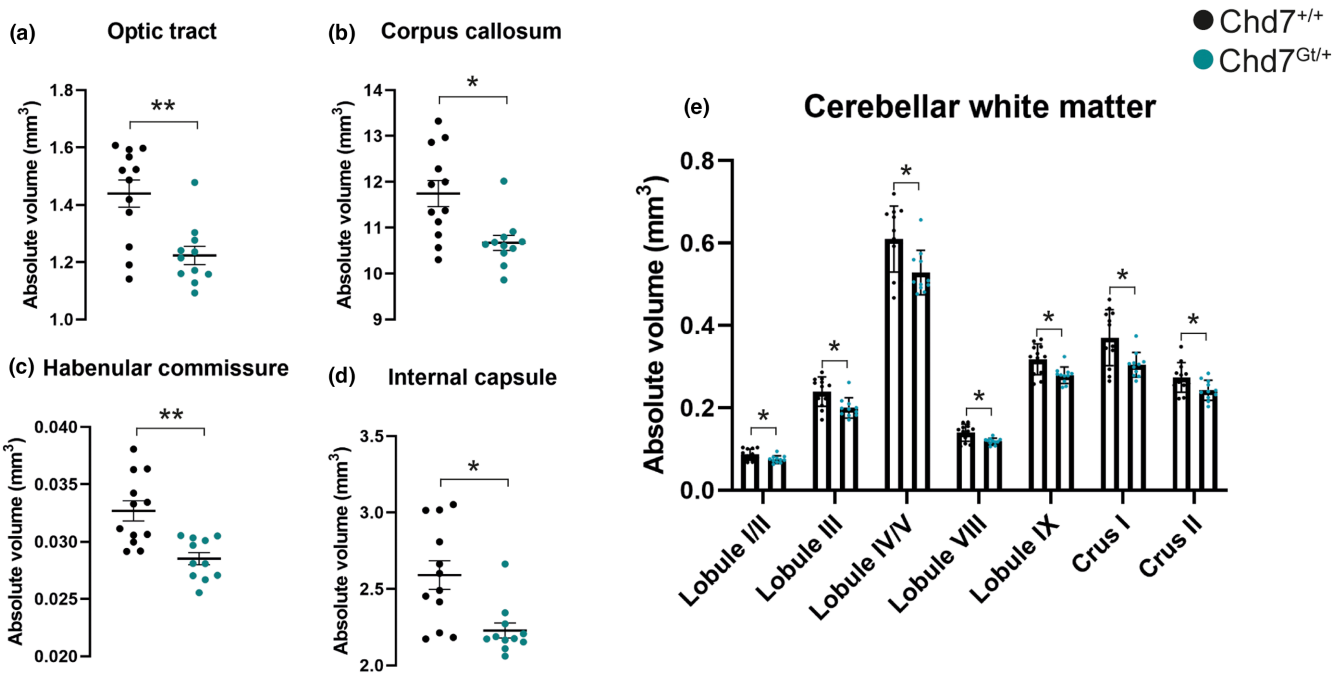

FIGURE 4 Loss of white matter volume in the brains of adult *Chd7*$^{Gt/+}$ mice. (a–d) Absolute volumetric differences (mm^3) between *Chd7*$^{+/+}$ (black) and *Chd7*$^{Gt/+}$ (teal) mice for total optic tract (a), corpus callosum (b), habenular commissure (c) and the internal capsule (d). (e) Absolute volumetric differences (mm^3) between *Chd7*$^{+/+}$ (black) and *Chd7*$^{Gt/+}$ (teal) mice in the white matter of the cerebellar lobules. All graphs are represented as mean ± SEM. Each point represents a biological replicate. *FDR < 5%, **FDR < 1%.

losses in FA and subsequent increased in MD and RD seem to indicate white matter integrity issues, i.e., axonal loss, myelination loss, and /or disorganization of the tract.

3.7 | Loss of mature oligodendrocytes and myelin in the corpus callosum of *Chd7*$^{Gt/+}$ mice

These MRI and DTI data suggested that there may be defects in the myelination of white matter tracts in the brains of adult *Chd7*$^{Gt/+}$ mice. Reductions in white matter myelin can arise from defects in multiple stages of oligodendrocyte specification, myelination or maintenance during postnatal development and ageing (Simons & Nave, 2016). Conditional deletion of *Chd7* from the oligodendrocyte precursor lineage causes defects in developmental myelination and in remyelination after injury (He et al., 2016). CHD7 has also been shown to play a role in the survival of oligodendrocyte precursor cells (OPCs) (Marie et al., 2018), raising the possibility that either or both defects in OPC differentiation or survival could underlie white matter deficits in *Chd7*$^{Gt/+}$ mice. To investigate this, we quantified the numbers of oligodendrocyte lineage cells present in the corpus callosum of P14 *Chd7*$^{Gt/+}$ and *Chd7*$^{+/+}$ mice (Figure 6a,b). We found a significant reduction in the numbers of OLIG2$^+$ oligodendrocyte lineage cells in the corpus callosum (Figure 6c). To further determine whether this loss of oligodendrocyte lineage cells is associated with a reduction in the numbers of mature oligodendrocytes OLIG2$^+$CC1$^+$ cells were quantified in the same region (Figure 6a,b). This analysis revealed a reduction in mature oligodendrocytes in *Chd7*$^{Gt/+}$ mice (Figure 6c), suggesting that there may be a deficit in oligodendrocyte specification during development in these mice. Finally, to determine whether loss of oligodendrocyte precursor cells contributes to the reduction in the OLIG2$^+$ population in the corpus callosum, we also quantified the numbers of OLIG2$^+$NKX2.2$^+$ cells (Figure 6d–f). We did not identify any difference in the number of oligodendrocyte precursor cells (Figure 6f), further supporting the proposition that the reduction in mature oligodendrocytes arises

FIGURE 5 Diffusion tensor imaging (DTI) of adult *Chd7*$^{Gt/+}$ mice. (a) Sagittal (a1) and coronal (a2) slice images from showing voxel-wise comparisons of fractional anisotropy present in adult (P60) *Chd7*$^{Gt/+}$ mice, differences relative to *Chd7*$^{+/+}$ are coloured according to the effect size scale from −1 to +1. (b) Sagittal (b1) and coronal (b2) slice images from showing voxel-wise comparisons of mean diffusivity present in adult (P60) *Chd7*$^{Gt/+}$ mice, differences relative to *Chd7*$^{+/+}$ are coloured according to the effect size scale from −1 to +1. (c) Sagittal (c1) and coronal (c2) slice images from showing voxel-wise comparisons of radial diffusivity present in adult (P60) *Chd7*$^{Gt/+}$ mice, differences relative to *Chd7*$^{+/+}$ are coloured according to the effect size scale from −1 to +1. (d) Regions with reduced fractional anisotropy between *Chd7*$^{+/+}$ (black) and *Chd7*$^{Gt/+}$ (teal) mice. (e) Regions with increased mean diffusivity between *Chd7*$^{+/+}$ (black) and *Chd7*$^{Gt/+}$ (teal) mice. (f) Regions with increased radial diffusivity between *Chd7*$^{+/+}$ (black) and *Chd7*$^{Gt/+}$ (teal) mice. Regions of interest in (a–c) are labelled as follows, Cb, cerebellum; CC, corpus callosum; Fb, fimbria; Hc, hippocampus; LX, cerebellar lobule X; PC, posterior commissure. All graphs are represented as mean ± SEM. Each point represents a biological replicate.

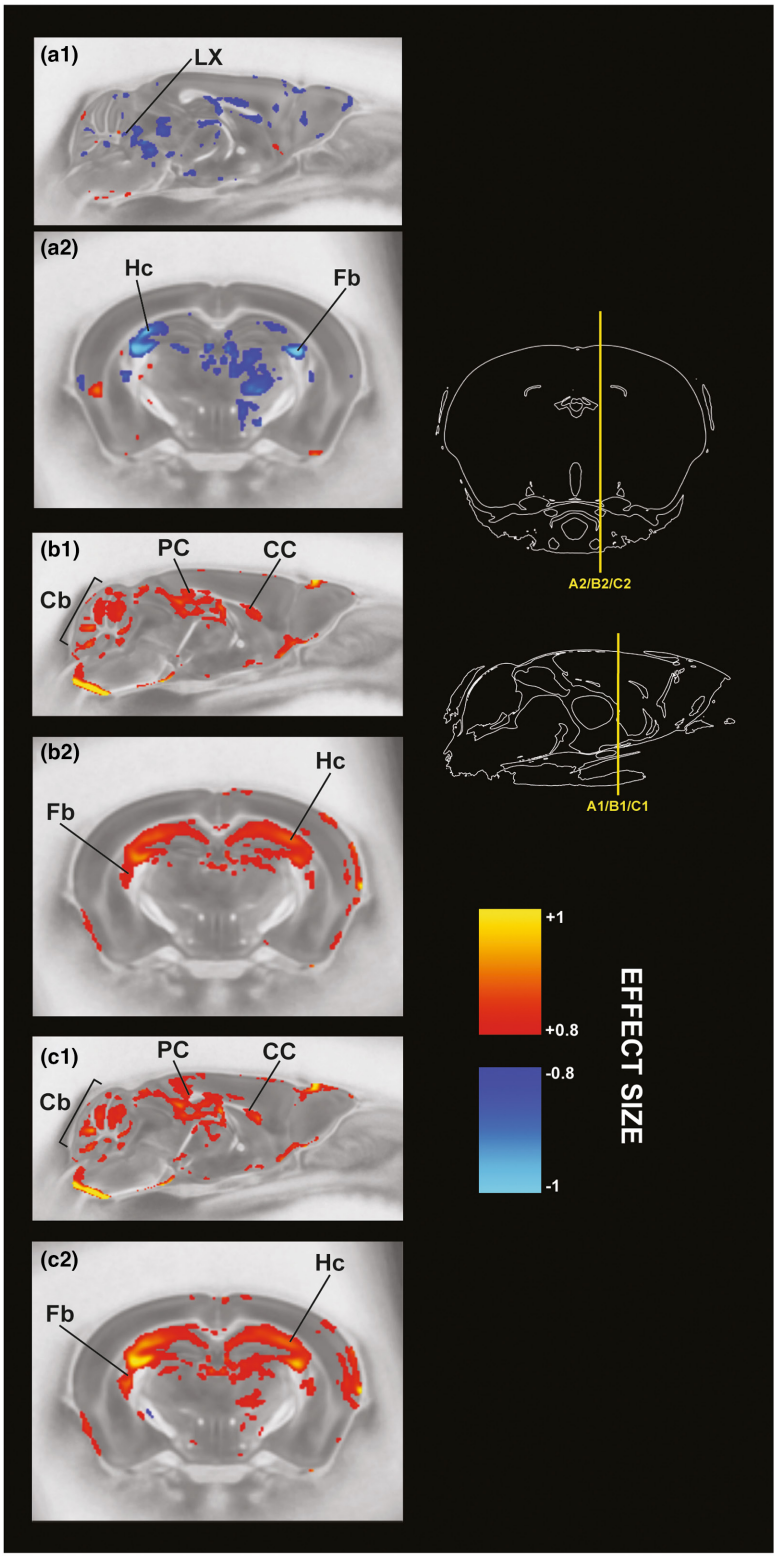
(a1)
LX
(a2)
Hc
Fb
(b1)
PC
CC
Cb
(b2)
Hc
Fb
(c1)
PC
CC
Cb
(c2)
Hc
Fb
A2/B2/C2
A1/B1/C1
+1
+0.8
-0.8
-1
EFFECT SIZE

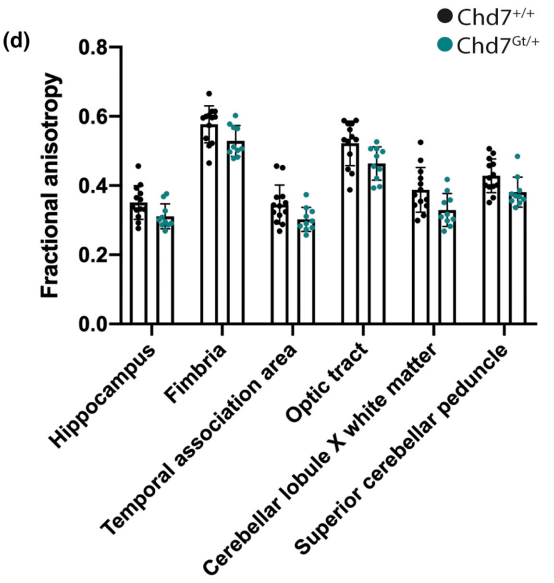
(d)
Chd7+/+
Chd7Gt/+
Fractional anisotropy
0.8
0.6
0.4
0.2
0.0
Hippocampus
Fimbria
Temporal association area
Optic tract
Cerebellar lobule X white matter
Superior cerebellar peduncle

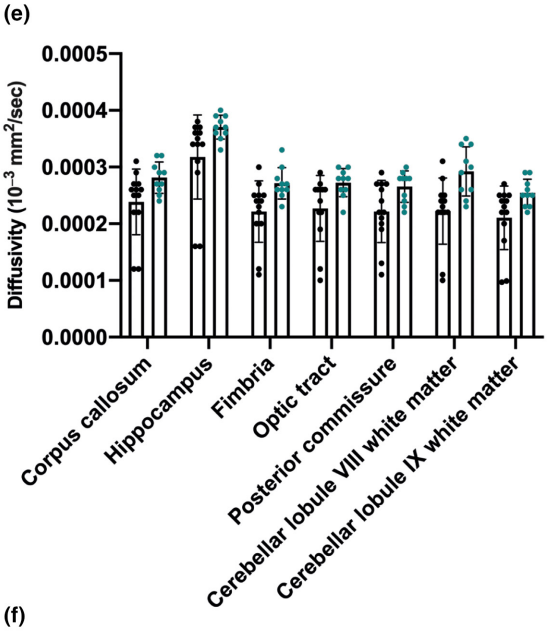
(e)
Diffusivity (10−3 mm2/sec)
0.0005
0.0004
0.0003
0.0002
0.0001
0.0000
Corpus callosum
Hippocampus
Fimbria
Optic tract
Posterior commissure
Cerebellar lobule VIII white matter
Cerebellar lobule IX white matter

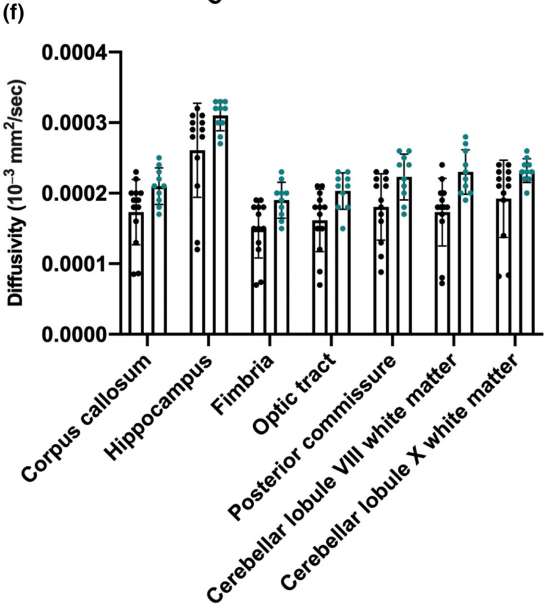
(f)
Diffusivity (10−3 mm2/sec)
0.0004
0.0003
0.0002
0.0001
0.0000
Corpus callosum
Hippocampus
Fimbria
Optic tract
Posterior commissure
Cerebellar lobule VIII white matter
Cerebellar lobule X white matter

from a deficit in oligodendrocyte differentiation and not a reduction in the number of oligodendrocyte precursor cells.

Oligodendrocytes contribute substantially to the number of glial cells in the mature brain, but other glial subtypes are also present within white matter in large numbers. To exclude the possibility that one of these, namely astrocytes, account for some amount of white matter volume loss in the corpus callosum, numbers of $SOX9^+/GFAP^+$ astrocytes were quantified in this region of $Chd7^{Gt/+}$ and $Chd7^{+/+}$ mice (Figure 6g–i). No significant change in astrocyte numbers was found, adding confidence to the idea that oligodendrocyte dysfunction underlies loss of volume in white matter structures (Figure 6i). The fact remained however that alterations present in mature oligodendrocyte cell number are unlikely to, in of themselves, account for the substantial volumetric abnormalities present within white matter structures. In order to obtain a more direct indication of myelination levels in the brains of $Chd7^{Gt/+}$ mice, immunohistochemistry for myelin basic protein (MBP) was performed and quantified within the corpus callosum (Figure 7a–c). This revealed a considerable loss in MBP (Figure 7c), further indicating that myelination is disrupted in $Chd7^{Gt/+}$ mice, and likely contributes substantially to loss of white matter volume in these mice.

4 | DISCUSSION

Here, we report the first comprehensive structural MRI and DTI examination of a *Chd7* haploinsufficient mouse model of CHARGE syndrome. We identified pervasive hypoplasia across the brain, with particularly striking defects in the cortex and white matter. To further probe the potential functional effects of white matter volume reductions, we performed DTI on the same cohorts of mice that underwent MRI. This revealed trends towards loss of white matter microstructure in the hippocampal formation, optic tract, cerebellum and commissural tracts, although these appeared less evident than the losses of volume identified in MRI, with none surviving FDR correction for multiple comparisons. To further delve into the potential causes of white matter anomalies in these mice, we performed targeted quantification of cells from the oligodendrocyte lineage, their precursors, and mature oligodendrocytes in the postnatal corpus callosum. This analysis revealed a substantial loss in mature oligodendrocyte cells but not their precursors postnatally, suggesting that the abnormalities in white matter present are likely caused by deficits in oligodendrocyte differentiation rather than reductions in numbers of oligodendrocyte precursor cells.

4.1 | Alterations in cerebral cortical volume may underlie symptoms of CHARGE syndrome

Our MRI analysis of *Chd7* haploinsufficient mice demonstrated diverse and widespread volumetric abnormalities across the cerebral cortex. When looking at absolute volumetric change, the entire cortex appeared to be reduced in volume to some degree. However, when looking at cortical areas relative to the total size of the cortex, we identified some regions that were in fact enlarged with respect to the proportion of the cortex that they occupy. Interestingly, the change in relative volume of these subdivisions appeared to follow a trend along the anterior–posterior axis whereby regions at the anterior were enlarged and regions towards the posterior, such as the auditory and visual cortices, were reduced in volume relative to total brain volume.

Deafness and blindness are highly prevalent in CHARGE syndrome, which represents one of the leading causes of congenital deafness and blindness in children (Ahn & Lee, 2013). Blindness and deafness in CHARGE syndrome have been classically solely attributed to defects in the sensory organs themselves, with few studies aimed at identifying whether consequent defects in the brain contribute. It is possible that structural defects in the areas of the cortex that process visual and auditory input could play a role in blindness and deafness in CHARGE syndrome. Feedback from the periphery during pre- and post-natal development is known to be important for the growth and myelination of sensory cortical areas and their corresponding axon tracts (Butler & Lomber, 2013; Emmorey et al., 2003), so loss of input due to sensorineural deafness or blindness may contribute to auditory and visual cortex hypoplasia. Mouse models of CHARGE syndrome, including $Chd7^{Gt/+}$ mice (Gage et al., 2015), have been shown to display eye defects expected to result in degrees of blindness (Gage et al., 2015) and $Chd7^{Gt/+}$ mice have been found to exhibit some degree of deafness (Hurd et al., 2007). Ablation of *Chd7* selectively in the cortex, sparing the sense organs and subsequent sensory testing may help determine the relation between auditory and visual cortex hypoplasia to deafness and blindness. Correspondingly, ablation of *Chd7* selectively in the sense organs followed by analysis of volumetric changes in the cortex by MRI would resolve whether disruptions in peripheral input have an effect on the growth of their associated cortical areas. These sensory inputs require transduction along white matter tracts, such as the optic tract, which was seen to be substantially reduced in volume in $Chd7^{Gt/+}$ mice. This raises the additional possibility that defects in white matter tract myelination could disrupt sensory inputs and contribute to volumetric abnormalities resultant of lost peripheral input.

It is also possible that deficits in the intrinsic growth of the cortex or increased cell death either during development or postnatally contribute to the loss of grey matter volume in the cortex. It will be important to ascertain whether these play a role in future by comprehensively assaying proliferation of progenitor populations in the developing cortex and by quantifying cell death during development and in the postnatal brain between birth and adulthood.

With respect to the relevance of these findings to known phenotypes of CHARGE syndrome, the hypoplasia in the auditory and visual cortices could present an important consideration when treating deaf-blindness in CHARGE patients, as treatments targeting peripheral sense-organ function may be limited by these brain abnormalities.

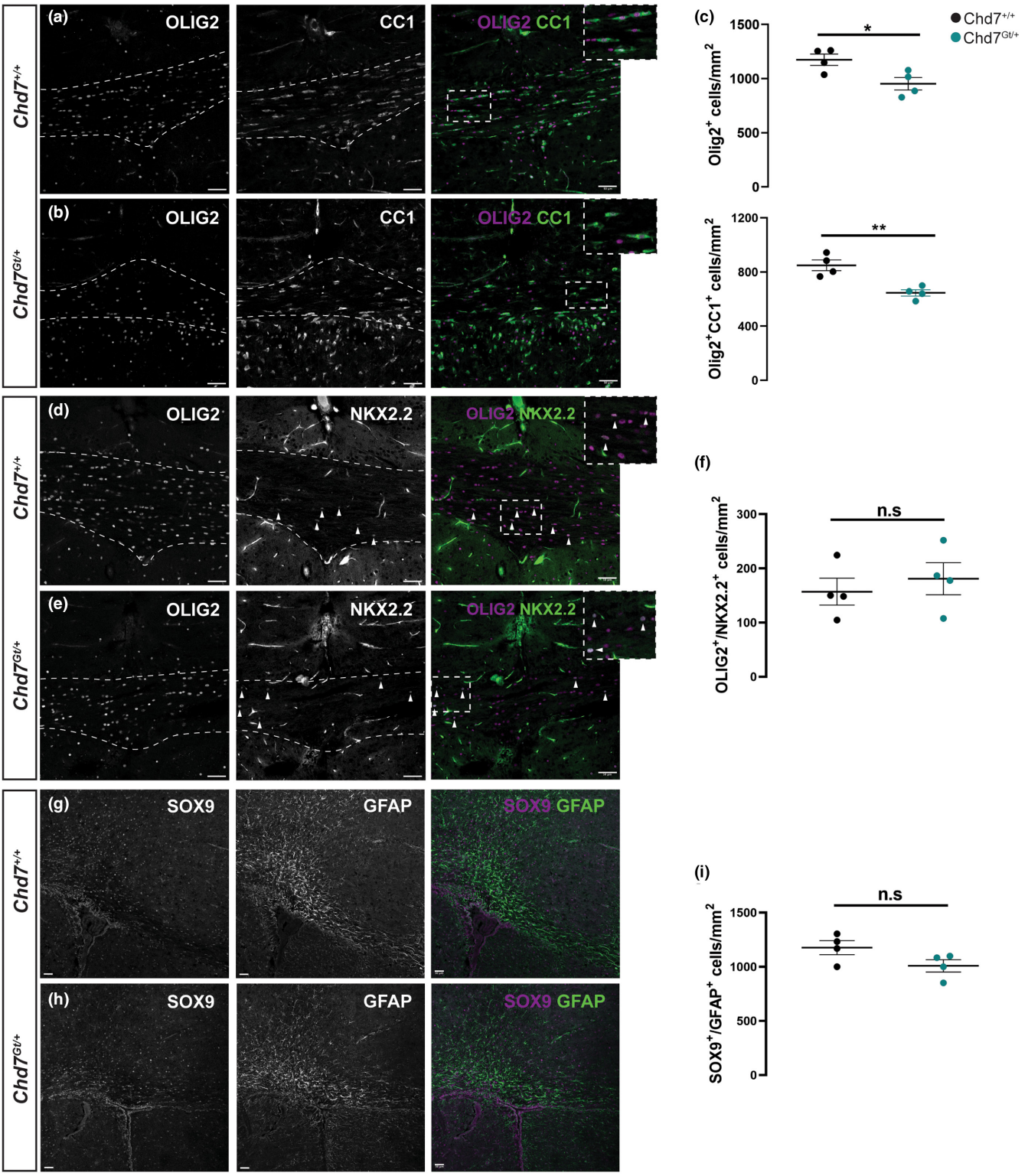

FIGURE 6 Reduced mature oligodendrocyte density in the corpus callosum of *Chd7*$^{Gt/+}$ mice. (a, b) Representative images of oligodendrocyte lineage cells (OLIG2$^+$ Magenta) and mature oligodendrocyte cells (OLIG2$^+$ Magenta, CC1$^+$ Green) in the corpus callosum of *Chd7*$^{+/+}$ (a) and *Chd7*$^{Gt/+}$ (b) mice at P14 ($n = 4$). (c) Quantification of immunostaining showing the number of OLIG2$^+$ oligodendrocyte lineage cells and mature oligodendrocyte cells (OLIG2$^+$ Magenta, CC1$^+$ Green) per mm^2 in *Chd7*$^{+/+}$ and *Chd7*$^{Gt/+}$ mice. (d, e) Representative images of oligodendrocyte precursor cells (OLIG2$^+$ Magenta, NKX2.2$^+$ Green) in the corpus callosum of *Chd7*$^{+/+}$ (d) and *Chd7*$^{Gt/+}$ (e) mice at P14 ($n = 4$). (f) Quantification of immunostaining showing the number of OLIG2$^+$NKX2.2$^+$ oligodendrocyte precursor cells per mm^2 in *Chd7*$^{+/+}$ and *Chd7*$^{Gt/+}$ mice. (g, h) Representative images of astrocytes (SOX9$^+$ Magenta, GFAP$^+$ Green) in the corpus callosum of *Chd7*$^{+/+}$ (a) and *Chd7*$^{Gt/+}$ (b) mice at P14 ($n = 4$). (i) Quantification of immunostaining showing the number of SOX9$^+$/GFAP$^+$ cells per mm^2 in *Chd7*$^{+/+}$ and *Chd7*$^{Gt/+}$ mice. All graphs are represented as mean ± SEM. Each point represents a biological replicate. *$p < 0.5$, ** $p < 0.1$.

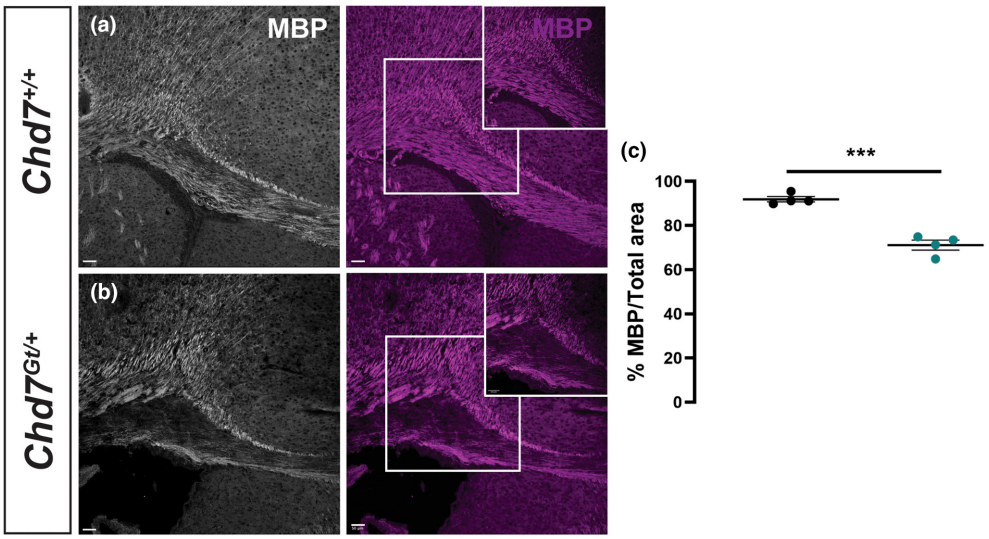

FIGURE 7 Reduced myelin basic protein (MBP) in the corpus callosum of *Chd7*$^{Gt/+}$ mice. (a, b) Representative images of myelin (MBP^{+} Magenta) in the corpus callosum of *Chd7*$^{+/+}$ (a) and *Chd7*$^{Gt/+}$ (b) mice at P14 ($n = 4$). (c) Quantification of immunostaining showing the amount of MBP^{+} myelin across the corpus callosum in *Chd7*$^{+/+}$ and *Chd7*$^{Gt/+}$ mice. All graphs are represented as mean ± SEM. Each point represents a biological replicate. $^{**}p < 0.01\%$.

4.2 | Brain volume defects in CHARGE syndrome may be partially attributable to general growth retardation in early postnatal life

Numerous deficits in brain volume have been noted in individuals with CHARGE syndrome, but the underlying causes remain unclear. Our analysis of body weight in *Chd7*$^{Gt/+}$ demonstrate a body growth retardation that then normalises between P14 and P21. This raises the possibility that some degree of the volumetric abnormalities present are secondary to a general growth retardation during early life. The hypoplasia we observe throughout the brain could thus be either a result of the delay in general growth but unable to normalise between early postnatal life and adulthood or independent of the early general growth retardation. It is known that CHARGE syndrome is, in most cases, associated with developmental delay (Hsu et al., 2014; Jongmans et al., 2006), which is thought to be resultant from feeding difficulties, sensory deficits and hospitalizations during early life. The possibility raised here that developmental delay could underlie brain volume abnormalities, which may be unable to normalise during adolescence, highlights the necessity of intervention during early life to ameliorate these factors. Further cranial imaging studies in CHARGE syndrome patients will allow for analysis of correlations between early life developmental delays and abnormalities in the mature brain.

It is also of interest to note that despite the presence of a developmental delay in body growth, we did not observe any alterations in skull size between adult *Chd7* haploinsufficient mice and wildtype controls. Coupled with the substantial loss of total brain volume, this could suggest that there would be an increase in the volume of the subarachnoid space present between the skull and brain. Although sometimes found to be benign (Kuruvilla, 2014), it has been noted to be an easily employable diagnostic tool in the identification of brain growth deficits in early postnatal infants (Yum et al., 2019), such as those often present in CHARGE syndrome.

4.3 | Reductions in white matter volume in CHARGE syndrome are potentially underpinned by defects in oligodendrocyte lineage progression

Abnormalities in white matter volume and defects in fibre tract integrity have been identified but not studied in CHARGE syndrome (Chen et al., 2019; Gregory et al., 2013; Shiohama et al., 2019). Our results suggest that a substantial proportion of the loss of brain volume identified both within this study and previously may be attributable to a loss of white matter, which was reduced to the same degree as grey matter in *Chd7*$^{gt/+}$ mice. We have identified widespread white matter hypoplasia in *Chd7* haploinsufficient mice across many regions in the cerebellum, as well as the optic tract and several major fiber tracts. Previous studies have characterised roles of CHD7 in white matter development, which provide conceivable mechanisms to underlie white matter loss in *Chd7* haploinsufficient mice. For instance, *Chd7* ablation from the precursors of the oligodendrocyte lineage unveiled vital roles for CHD7 in both the onset of myelination and the process of remyelination that occurs after injury (He et al., 2016). The authors determined that CHD7 is a key regulator of the transition of fate from oligodendrocyte precursors to oligodendrocytes (He et al., 2016). Our results indicate that reduction in white matter volume in *Chd7*$^{Gt/+}$ mice is consistent with similar mechanisms, as we find decreases in the numbers of mature oligodendrocyte cells and myelination as early as P14.

A key role has been described for CHD7 in the regulation of oligodendrocyte precursor cell survival and differentiation, through the

maintenance of heterochromatin around the *p53* promoter (Marie et al., 2018). In contrast to reductions in postnatal OPC number in the corpus callosum seen by Marie et al. (2018) at P7 in mice with *Chd7* ablated from the oligodendrocyte lineage, we did not observe any loss of OPCs in the corpus callosum of juvenile (P14) $Chd7^{Gt/+}$ mice. However, as the MRI/DTI measurements were done on adult mice (P60), it remains possible that a loss of oligodendrocyte precursor cells could arise later in life. Additionally, p53-mediated apoptosis of OPCs was identified in a *Chd7* null condition and P53 activation is likely highly sensitive to dosage of *Chd7* expression, as has been observed in *Chd8* mutants, where haploinsufficiency is not associated with significant P53 activation (Hurley et al., 2021). It is also possible that some recovery of OPC numbers occurs between P7 and P14. Moreover, it is also conceivable that although we find a substantial loss of myelin at P14, that this too may recover to some extent by adulthood. Longitudinal analysis of oligodendrocyte development and myelination across the brain regions effected in $Chd7^{Gt/+}$ mice will be key to comprehensively define the aberrant mechanisms underlying the loss of myelin observed in adults. Together, our results suggest that defects in oligodendrocyte precursor differentiation and subsequent production of myelin, rather than loss of OPCs, may underlie white matter dysfunction in CHARGE syndrome patients.

In conclusion, we have identified widespread and severe hypoplasia of structures across the brains of adult *Chd7* haploinsufficient mice. Our analyses demonstrate for the first time in a mouse model for CHARGE syndrome that biallelic expression of *Chd7* is required for the normal growth and maturation of the brain. The alterations in white matter reported in CHARGE syndrome patients are expected to have a substantial impact on long-range connectivity in the brain. Our findings suggest that defects may be present in regions of the cerebellum and hippocampus that share functional connections with the prefrontal cortex, known to be important for proper executive functions, which are known to be specifically disturbed in CHARGE syndrome (Hartshorne et al., 2007; Nicholas, 2005). Further study into the roles of CHD7 in oligodendrocyte lineage specification, maturation, maintenance and the process of myelination alongside more comprehensive neuropsychiatric phenotype-linked cranial imaging and tractography studies in CHARGE syndrome patients will be key to fully understand the causes and functional consequences of myelin loss.

AUTHOR CONTRIBUTIONS

The study was designed by APAD and MAB. Animal experiments and tissue collections were performed by APAD. Neuroimaging was performed by JE and JPL. Immunostaining and quantifications were performed by LR and JKH. Skull analysis was performed by YR and JBAG. APAD analysed the data, generated the figures and wrote the manuscript with MAB, with input from all authors.

ACKNOWLEDGMENTS

We thank Peter Scambler (UCL Great Ormond Street Institute of Child Health) for the $Chd7^{gt/+}$ mouse line, BSU staff at King's College London for animal husbandry, and the Anatomical Society (PhD studentship to APD) and the CHARGE syndrome foundation (Pilot grant to MAB) for funding. All animal work was approved by the institutional ethical review board (AWERB) at King's College London and the UK Home Office (Project licence P8DC5B496). We would also like to acknowledge funding from the Ontario Brain Institute (OBI) (JE and JPL).

CONFLICT OF INTEREST STATEMENT

The authors have no competing interests to declare.

DATA AVAILABILITY STATEMENT

The data that support the findings of this study are available from the corresponding author upon reasonable request.

ORCID

Alex P. A. Donovan https://orcid.org/0000-0002-7418-2447
Lauren Rosko https://orcid.org/0000-0002-6620-0879
Jeremy B. A. Green https://orcid.org/0000-0002-6102-2620
M. Albert Basson https://orcid.org/0000-0001-9834-7528

REFERENCES

Ahn, J.H. & Lee, K.S. (2013) Outcomes of cochlear implantation in children with CHARGE syndrome. *Acta Oto-Laryngologica*, 133(11), 1148–1153. Available from: https://doi.org/10.3109/00016489.2013.814155

Bernstein, V. & Denno, L.S. (2005) Repetitive behaviors in CHARGE syndrome: differential diagnosis and treatment options. *American journal of medical genetics. Part A*, 133(3), 232–239. Available from: https://doi.org/10.1002/ajmg.a.30542

Blake, K.D., Davenport, S.L.H., Hall, B.D., Hefner, M.A., Pagon, R.A., Williams, M.S. et al. (1998) Charge association: an update and review for the primary pediatrician. *Clinical Pediatrics*, 37(3), 159–174. Available from: https://doi.org/10.1177/000992289803700302

Blake, K.D. & Prasad, C. (2006) CHARGE syndrome. *Orphanet Journal of Rare Diseases*, 1(1), 1–8. Available from: https://doi.org/10.1186/1750-1172-1-34

Butler, B.E. & Lomber, S.G. (2013) Functional and structural changes throughout the auditory system following congenital and early-onset deafness: implications for hearing restoration. *Frontiers in Systems Neuroscience*, 7(November), 1–17. Available from: https://doi.org/10.3389/fnsys.2013.00092

Chamberlain, K.A., Chapey, K.S., Nanescu, S.E. & Huang, J.K. (2017) Creatine enhances mitochondrial-mediated oligodendrocyte survival after demyelinating injury. *Journal of Neuroscience*, 37(6), 1479–1492. Available from: https://doi.org/10.1523/JNEUROSCI.1941-16.2016

Chen, X., Yan, K., Gao, Y., Wang, H., Chen, G., Wu, B. et al. (2019) Feeding difficulty is the dominant feature in 12 Chinese newborns with CHD7 pathogenic variants. *BMC Medical Genetics*, 20(1), 1–10. Available from: https://doi.org/10.1186/s12881-019-0813-z

de Geus, C.M., Free, R.H., Verbist, B.M., Sival, D.A., Blake, K.D., Meiners, L.C. et al. (2017) Guidelines in CHARGE syndrome and the missing link: cranial imaging. *American Journal of Medical Genetics, Part C: Seminars in Medical Genetics*, 175(4), 450–464. Available from: https://doi.org/10.1002/ajmg.c.31593

Donovan, A.P.A., Yu, T., Ellegood, J., Riegman, K.L.H., de Geus, C., van Ravenswaaij-Arts, C. et al. (2017) Cerebellar vermis and midbrain hypoplasia upon conditional deletion of Chd7 from the embryonic mid-hindbrain region. *Frontiers in Neuroanatomy*, 11(October), 1–9. Available from: https://doi.org/10.3389/fnana.2017.00086

Dorr, A.E., Lerch, J.P., Spring, S., Kabani, N. & Henkelman, R.M. (2008) High resolution three-dimensional brain atlas using an average

magnetic resonance image of 40 adult C57Bl/6J mice. *NeuroImage*, 42, 60–69. Available from: https://doi.org/10.1016/j.neuroimage.2008.03.037

Ellegood, J., Yee, Y., Kerr, T.M., Muller, C.L., Blakely, R.D., Henkelman, R.M. et al. (2018) Analysis of neuroanatomical differences in mice with genetically modified serotonin transporters assessed by structural magnetic resonance imaging. *Molecular Autism*, 9(1), 1–12. Available from: https://doi.org/10.1186/s13229-018-0210-z

Emmorey, K., Allen, J.S., Bruss, J., Schenker, N. & Damasio, H. (2003) A morphometric analysis of auditory brain regions in congenitally deaf adults. *Proceedings of the National Academy of Sciences of the United States of America*, 100(17), 10049–10054. Available from: https://doi.org/10.1073/pnas.1730169100

Feng, W., Kawauchi, D., Körkel-Qu, H., Deng, H., Serger, E., Sieber, L. et al. (2017) Chd7 is indispensable for mammalian brain development through activation of a neuronal differentiation programme. *Nature Communications*, 8, 14758. Available from: https://doi.org/10.1038/ncomms14758

Gage, P.J., Hurd, E.A. & Martin, D.M. (2015) Mouse models for the dissection of CHD7 functions in eye development and the molecular basis for ocular defects in CHARGE syndrome. *Investigative Ophthalmology and Visual Science*, 56(13), 7923–7930. Available from: https://doi.org/10.1167/iovs.15-18069

Gregory, L.C., Gevers, E.F., Baker, J., Kasia, T., Chong, K., Josifova, D.J. et al. (2013) Structural pituitary abnormalities associated with CHARGE syndrome. *Journal of Clinical Endocrinology and Metabolism*, 98(4), 737–743. Available from: https://doi.org/10.1210/jc.2012-3467

Hartshorne, T.S., Grialou, T.L. & Parker, K.R. (2005) Autistic-like behavior in CHARGE syndrome. *American Journal of Medical Genetics*, 133 A(3), 257–261. Available from: https://doi.org/10.1002/ajmg.a.30545

Hartshorne, T.S., Nicholas, J., Grialou, T.L. & Russ, J.M. (2007) Executive function in charge syndrome. *Child Neuropsychology*, 13(4), 333–344. Available from: https://doi.org/10.1080/09297040600850944

He, D., Marie, C., Zhao, C., Kim, B., Wang, J., Deng, Y. et al. (2016) Chd7 cooperates with Sox10 and regulates the onset of CNS myelination and remyelination. *Nature Neuroscience*, 19(5), 678–689. Available from: https://doi.org/10.1038/nn.4258

Hoch, M.J., Patel, S.H., Jethanamest, D., Win, W., Fatterpekar, G.M., Roland, J.T. et al. (2017) Head and neck MRI findings in CHARGE syndrome. *American Journal of Neuroradiology*, 38(12), 2357–2363. Available from: https://doi.org/10.3174/ajnr.A5297

Hsu, P., Ma, A., Wilson, M., Williams, G., Curotta, J., Munns, C.F. et al. (2014) CHARGE syndrome: a review. *Journal of Paediatrics and Child Health*, 50(7), 504–511. Available from: https://doi.org/10.1111/jpc.12497

Hurd, E.A., Capers, P.L., Blauwkamp, M.N., Adams, M.E., Raphael, Y., Poucher, H.K. et al. (2007) Loss of Chd7 function in gene-trapped reporter mice is embryonic lethal and associated with severe defects in multiple developing tissues. *Mammalian Genome*, 18(2), 94–104. Available from: https://doi.org/10.1007/s00335-006-0107-6

Hurley, S., Mohan, C., Suetterlin, P., Ellingford, R., Riegman, K.L.H., Ellegood, J. et al. (2021) Distinct, dosage-sensitive requirements for the autism-associated factor CHD8 during cortical development. *Molecular Autism*, 12(1), 16. Available from: https://doi.org/10.1186/s13229-020-00409-3

Janssen, N., Bergman, J.E.H., Swertz, M.A., Tranebjaerg, L., Lodahl, M., Schoots, J. et al. (2012) Mutation update on the CHD7 gene involved in CHARGE syndrome. *Human Mutation*, 33(8), 1149–1160. Available from: https://doi.org/10.1002/humu.22086

Johansson, M., Råstam, M., Billstedt, E., Danielsson, S., Strömland, K., Miller, M. et al. (2005) Autism spectrum disorders and underlying brain pathology in CHARGE association. *Developmental Medicine and Child Neurology*, 48(01), 40. Available from: https://doi.org/10.1017/s0012162206000090

Jones, D.K., Horsfield, M.A. & Simmons, A. (1999) Optimal strategies for measuring diffusion in anisotropic systems by magnetic resonance imaging. *Magnetic Resonance in Medicine*, 42, 515–525. Available from: https://doi.org/10.1002/(SICI)1522-2594(199909)42:3<515::AID-MRM14>3.0.CO;2-Q

Jongmans, M.C., Admiraal, R.J., van der Donk, K.P., Vissers, L.E., Baas, A.F., Kapusta, L. et al. (2006) CHARGE syndrome: the phenotypic spectrum of mutations in the CHD7 gene. *Journal of Medical Genetics*, 43(4), 306–314. Available from: https://doi.org/10.1136/jmg.2005.036061

Kuruvilla, L.C. (2014) Benign enlargement of sub-arachnoid spaces in infancy. *Journal of Pediatric Neurosciences*, 9(2), 129–131. Available from: https://doi.org/10.4103/1817-1745.139309

Lerch, J.P., Carroll, J.B., Dorr, A., Spring, S., Evans, A.C., Hayden, M.R. et al. (2008) Cortical thickness measured from MRI in the YAC128 mouse model of Huntington's disease. *NeuroImage*, 41(2), 243–251. Available from: https://doi.org/10.1016/j.neuroimage.2008.02.019

Lerch, J.P., Sled, J.G. & Henkelman, R.M. (2011) MRI phenotyping of genetically altered mice. *Magnetic Resonance Neuroimaging*, 711, 349–361. Available from: https://doi.org/10.1007/978-1-61737-992-5_17

Lerch, J.P., van der Kouwe, A.J.W., Raznahan, A., Paus, T., Johansen-Berg, H., Miller, K.L. et al. (2017) Studying neuroanatomy using MRI. *Nature Neuroscience*, 20(3), 314–326. Available from: https://doi.org/10.1038/nn.4501

Lin, A.E., Siebert, J.R. & Graham, J.M., Jr. (1990) Central nervous system malformations in the CHARGE association. *American Journal of Medical Genetics*, 37, 304–310. Available from: https://doi.org/10.1002/ajmg.1320370303

Marie, C., Clavairoly, A., Frah, M., Hmidan, H., Yan, J., Zhao, C. et al. (2018) Oligodendrocyte precursor survival and differentiation requires chromatin remodeling by Chd7 and Chd8. *Proceedings of the National Academy of Sciences of the United States of America*, 115(35), E8246–E8255. Available from: https://doi.org/10.1073/pnas.1802620115

Nicholas, J. (2005) Can specific deficits in executive functioning explain the behavioral characteristics of CHARGE syndrome: a case study. *American journal of medical genetics. Part A*, 133, 300–305. Available from: https://doi.org/10.1002/ajmg.a.30558

Nieman, B.J., Flenniken, A.M., Adamson, S.L., Henkelman, R.M. & Sled, J.G. (2006) Anatomical phenotyping in the brain and skull of a mutant mouse by magnetic resonance imaging and computed tomography. *Physiological Genomics*, 24, 154–162. Available from: https://doi.org/10.1152/physiolgenomics.00217.2005

Randall, V., McCue, K., Roberts, C., Kyriakopoulou, V., Beddow, S., Barrett, A.N. et al. (2009) Great vessel development requires biallelic expression of Chd7 and Tbx1 in pharyngeal ectoderm in mice. *Journal of Clinical Investigation*, 119(11), 3301–3310. Available from: https://doi.org/10.1172/JCI37561

Richtsmeier, J.T. & Flaherty, K. (2013) Hand in glove: brain and skull in development and dysmorphogenesis. *Acta Neuropathologica*, 125(4), 469–489. Available from: https://doi.org/10.1007/s00401-013-1104-y

Russell-Eggitt, I.M., Blake, K.D., Taylor, D.S. & Wyse, R.K. (1990) The eye in the CHARGE association. *The British Journal of Ophthalmology*, 74, 421–426. Available from: https://doi.org/10.1136/bjo.74.7.421

Sanlaville, D., Etchevers, H.C., Gonzales, M., Martinovic, J., Clément-Ziza, M., Delezoide, A.L. et al. (2006) Phenotypic spectrum of CHARGE syndrome in fetuses with CHD7 truncating mutations correlates with expression during human development. *Journal of Medical Genetics*, 43(3), 211–217. Available from: https://doi.org/10.1136/jmg.2005.036160

Shiohama, T., McDavid, J., Levman, J. & Takahashi, E. (2019) Quantitative brain morphological analysis in CHARGE syndrome. *NeuroImage: Clinical*, 23(May), 101866. Available from: https://doi.org/10.1016/j.nicl.2019.101866

Simons, M. & Nave, K.A. (2016) Oligodendrocytes: myelination and axonal support. *Cold Spring Harbor Perspectives in Biology*, 8(1), a020479. Available from: https://doi.org/10.1101/cshperspect.a020479

Smith, I.M., Nichols, S.L., Issekutz, K. & Blake, K. (2005) Behavioral profiles and symptoms of autism in CHARGE syndrome: preliminary Canadian epidemiological data. *American Journal of Medical Genetics. Part A*, 133(3), 248–256. Available from: https://doi.org/10.1002/ajmg.a.30544

Sohn, Y.B., Ko, J.M., Shin, C.H., Yang, S.W., Chae, J.H. & Lee, K.A. (2016) Cerebellar vermis hypoplasia in CHARGE syndrome: clinical and molecular characterization of 18 unrelated Korean patients. *Journal of Human Genetics*, 61(3), 235–239. Available from: https://doi.org/10.1038/jhg.2015.135

Steadman, P.E., Ellegood, J., Szulc, K.U., Turnbull, D.H., Joyner, A.L., Henkelman, R.M. et al. (2014) MRI of genetic mouse model's cerebellum. *Autism Research*, 7, 124–137. Available from: https://doi.org/10.1002/aur.1344

Toussaint, N., Redhead, Y., Vidal-García, M., Lo Vercio, L., Liu, W., Fisher, E.M.C. et al. (2021) A landmark-free morphometrics pipeline for high-resolution phenotyping: application to a mouse model of down syndrome. *Development*, 148(18), dev188631. Available from: https://doi.org/10.1242/dev.188631

Ullmann, J.F., Watson, C., Janke, A.L., Kurniawan, N.D. & Reutens, D.C. (2013) A segmentation protocol and MRI atlas of the C57BL/6J mouse neocortex. *NeuroImage*, 78, 196–203. Available from: https://doi.org/10.1016/j.neuroimage.2013.04.008

Verloes, A. (2005) Updated diagnostic criteria for CHARGE syndrome: a proposal. *American journal of medical genetics. Part A*, 133(3), 306–308. Available from: https://doi.org/10.1002/ajmg.a.30559

Vissers, L.E.L.M., van Ravenswaaij, C.M.A., Admiraal, R., Hurst, J.A., de Vries, B.B.A., Janssen, I.M. et al. (2004) Mutations in a new member of the chromodomain gene family cause CHARGE syndrome. *Nature Genetics*, 36(9), 955–957. Available from: https://doi.org/10.1038/ng1407

Wachtel, L.E., Hartshorne, T.S. & Dailor, A.N. (2007) Psychiatric diagnoses and psychotropic medications in CHARGE syndrome: a pediatric survey. *Journal of Developmental and Physical Disabilities*, 19(5), 471–483. Available from: https://doi.org/10.1007/s10882-007-9064-6

Whittaker, D.E., Kasah, S., Donovan, A.P.A., Ellegood, J., Riegman, K.L.H., Volk, H.A. et al. (2017) Distinct cerebellar foliation anomalies in a CHD7 haploinsufficient mouse model of CHARGE syndrome. *American Journal of Medical Genetics, Part C: Seminars in Medical Genetics*, 175(4), 465–477. Available from: https://doi.org/10.1002/ajmg.c.31595

Whittaker, D.E., Riegman, K.L.H., Kasah, S., Mohan, C., Yu, T., Sala, B.P. et al. (2017) The chromatin remodeling factor CHD7 controls cerebellar development by regulating reelin expression. *Journal of Clinical Investigation*, 127(3), 874–887. Available from: https://doi.org/10.1172/JCI83408

Yu, T., Meiners, L.C., Danielsen, K., Wong, M.T.Y., Bowler, T., Reinberg, D. et al. (2013) Deregulated FGF and homeotic gene expression underlies cerebellar vermis hypoplasia in CHARGE syndrome. *eLife*, 2013(2), 8–10. Available from: https://doi.org/10.7554/eLife.01305

Yum, S.K., Im, S.A., Seo, Y.M. & Sung, I.K. (2019) Enlarged subarachnoid space on cranial ultrasound in preterm infants: neurodevelopmental implication. *Scientific Reports*, 9, 19072. Available from: https://doi.org/10.1038/s41598-019-55604-x

SUPPORTING INFORMATION

Additional supporting information can be found online in the Supporting Information section at the end of this article.

How to cite this article: Donovan, A.P.A., Rosko, L., Ellegood, J., Redhead, Y., Green, J.B.A., Lerch, J.P. et al. (2023) Pervasive cortical and white matter anomalies in a mouse model for CHARGE syndrome. *Journal of Anatomy*, 243, 51–65. Available from: https://doi.org/10.1111/joa.13856